RSC Advances

ROYAL SOCIETY OF CHEMISTRY

www.rsc.org/advances

Electric, Magnetic and Optical Limiting (short pulse and Ultrafast) Studies in Phase Pure (1-x)$BiFeO_3$-x$NaNbO_3$ Multiferroic Nanocomposite Synthesized by Pechini Method

Rehana P Ummer,[a] P. Sreekanth,[d] B. Raneesh,[b] Reji Philip,[d] Didier Rouxel[e], Sabu Thomas[b,c] and Nandakumar Kalarikkal[a,b]

[a]School of Pure and Applied Physics

[b]International and Inter University Centre for Nanoscience and Nanotechnology

[c]School of Chemical Sciences

Mahatma Gandhi University, Kottayam, Kerala-686560, India

[d]Ultrafast and Nonlinear Optics Lab, Light and Matter Physics Group, Raman Research Institute, Bangalore, 560080, India

[e]Institut Jean Lamour - UMR CNRS 7198, Faculté des Sciences et Techniques, Campus Victor Grignard - BP 70239, 54506,Vandoeuvre-les-Nancy Cedex, France

Abstract

Perovskite (1-x)$BiFeO_3$-x$NaNbO_3$ nanocomposite was successfully synthesized by Pechini method and crystallographic information was obtained from XRD and TEM analysis. Structural analysis using XRD and TEM shows that phase pure samples were obtained with reduced particle size. The observations encountered reveal that particle size plays a crucial role in deciding the electric and magnetic properties. The multiferroic character of nanoparticles is confirmed through magneto electric (ME) coupling studies. The good coexistence of ferroelectric and ferromagnetic behaviors in the composite provides the possibility to achieve a measurable ME effect. The highest value of the magneto electric coefficient (α) is observed for x=0.1 (α=0.13 $Vcm^{-1}Oe^{-1}$) and it reduces for higher x values. Magnetization measurements for x=0.1 show small hysteresis at 6 K which also confirms the presence of magnetic phase at low temperature while the usual antiferromagnetic behavior of BFO is found at 300 K. The reduced size and absence of impurity could be the reason for the enhancement in electrical property. Low loss tangent values observed in the samples is a remarkable improvement. Open aperture Z-scan measurements reveal a nonlinear absorption behavior, which results in good optical limiting when excited with short pulse (nanosecond) as well as ultrafast (femtosecond) laser pulses.

Keywords: Multiferroic, Magnetoelectric coupling, Optical limiting

E-mail: nkkalarikkal@mgu.ac.in, Tel: +919447671962, Fax: +91481-2731669, Mail address: School of Pure and Applied Physics, Mahatma Gandhi University, Kottayam, Kerala 686 560, India

1. Introduction

In recent years, multiferroic materials is a time honored research subject due to its potential applications for the future technology in information storage, sensors, optical limiters[1-5] and for exploring physical phenomena of the coupling mechanism between electric and magnetic order parameters.[6-9] The combination of more than one ferroic property in single material is also interesting and fascinating. There are few materials that can exhibit both magnetization and electric polarization together. Among them $BiFeO_3$ (BFO) is the most extensively studied compound.[10] It is one of the well known single phase multiferroic material with distorted perovskite (ABO_3) structure. The perovskite $BiFeO_3$ possesses a ferroelectric transition Tc~830° C and antiferromagnetic transition at T_N~370°C. BFO is unique amongst many multiferroics, as its ferroelectric and magnetic transition temperatures are well above the room temperature raising the possibility of potential devices based on magneto electric (M-E) coupling operating at room temperature.[7] The BFO also has other exceptional applications such as photo catalytic, ultrafast, optoelectronic and infrared detector devices due to its small band gap.[11,12] In spite of the above qualities, this material has some inherent problems that limit its applications. For example, BFO has high leakage current that allows current to pass through it when a high voltage is applied. It has high dielectric loss and low polarization. In order to solve these inherent problems, several attempts have been made in the recent past, such as doping it with rare earth elements like samarium, lanthanum etc. at the appropriate atomic sites and/or fabricating its composites. $NaNbO_3$ is one of the representative lead-free piezoelectric perovskite oxides which have large practical importance and composite with BFO is of considerable interest.[13] Multiphase multiferroics are successful approach to overcome the limitations of single phase materials such as the small magneto electric coupling.[2,4,13-17] The composites of BFO made with $NaNbO_3$ showed reduction in the leakage current and enhancement of electric properties.[18] A lot of attempts have been concentrated on the research and development of high performance lead-free piezoelectric ceramics such as alkali niobates.

$NaNbO_3$ is one among them which give rise to a set of phase transitions.[19,20] $NaNbO_3$ is highly soluble in any solid solution of perovskite materials.[21]

We have prepared solid solutions of BFO and $NaNbO_3$ in different composition with a general formula $(Bi_{1-x}Na_x)$ $(Fe_{1-x}Nb_x)O_3$ where x = 0, 0.1, 0.5 and 0.7 using sol-gel reaction. In this paper, we detail the electric, magnetic and optical study of the as prepared samples. As per our knowledge there is no previous work reported on the physical properties of nano structured $BiFeO_3$-$NaNbO_3$ composite.[25] Nonlinear study is previously observed on Bismuth ferrite by Monte Carlo simulation and density functional theory.[27] Also Bismuth based glasses exhibit large third order optical nonlinearity in oxide glasses, indicating they are promising materials for nonlinear optical devices.[23]

2. Materials and methods

The solid solution ceramics of $Bi_{1-x}Na_xFe_{1-x}Nb_xO_3$ with x=0, 0.1, 0.5, and 0.7 were prepared by modified sol-gel method called pechini method.[24,26]AR grade of Ammonium Niobate Oxalate (Sigma-aldrich > 99 % pure), $Bi(NO_3)_3$ (Sigma-aldrich > 99 % pure), $Fe(NO_3)_3$(Sigma-aldrich > 99 % pure), $NaNbO_3$ (Sigma-aldrich > 99 % pure) were used as raw materials. Firstly, the raw materials were carefully weighted in stoichiometric ratio and dissolved in Citric acid aqueous solution (in 1:1 molar ratio with respect to the total metal cation) and pH value was adjusted to 5 using NH_3OH. The clear solution thus obtained was dried at 100^o C to form gel and the gel was burnt at 500^o C to get the ceramic powders. After that the powder was ground and pressed into pellets. Finally the pellets were sintered at 850^o C for 1 hour to get the final sample. The crystal structures of the samples were examined by Phillips X'Pert Pro XRD with Cu-Kα radiation (1.54056 Å). Step scanned powder XRD data was collected in the 2θ range 10º-80º at room temperature on the finely ground sample. Detailed structural analysis was performed using Scanning Electron Microscope (JEOL JSM 6390) and Transmission Electron Microscope (JEOL JEM 2100). The relative dielectric constant ε, and dissipation factor tan ɗ at room temperature were measured using an LCR meter (Agilent E4980A). The magnetoelectric coupling was determined using a lock in amplifier technique and magnetization measurements were performed using SQUID magnetometer. The absorption spectrum was taken using a UV-VIS

spectrophotometer (SHIMADZU, UV-2450). The nonlinear optical measurements were carried out using the conventional open aperture Z-scan technique. The powder samples suspended in DMF by sonication were taken in a 1 mm cuvette. For excitation, 5 ns laser pulses were obtained from a frequency doubled Nd:YAG laser (Minilite Continuum, 532 nm) and 100 fs pulses were obtained from a regeneratively amplified mode-locked Ti-Sapphire laser (Spectra physics, 800 nm). In the Z-scan set up, the laser beam is focused using a lens and the sample is translated along the beam axis (z axis) through the focus (z=0). At each position 'z' the sample sees a different laser fluence, and the transmission is measured using a pyroelectric laser energy probe which is placed after the sample. Inorder to monitor the pulse-to-pulse laser energy variation we used a reference beam picked off from the main beam. All measurements were done in the single-shot mode and there is an interval of about 10 seconds between successive laser pulses. Using the data obtained from Z-scan measurements, nonlinear optical parameters could be calculated by numerically fitting the data points using the appropriate nonlinear transmission equations.

3. Results and discussion

3.1 Structural Analysis

Fig. 1 shows the XRD pattern of (1-x)$BiFeO_3$-x$NaNbO_3$ composite system for x=0, 0.1, 0.5 and 0.7 at room temperature . The peaks that correspond to $BiFeO_3$ and $NaNbO_3$ are indicated by B and N respectively. XRD data reveals that both the phases of $BiFeO_3$ and $NaNbO_3$ are present in the composite system. Non-perovskite phases such as $Bi_2Fe_4O_9$ and Bi_2O_3/Fe_2O_3 were not detected in the XRD spectrum which is a common occurrence when we adopt other techniques for the preparation. In the XRD spectra it could be obeserved that as x increases the peaks corresponding to orthorhombic $NaNbO_3$ appear. Also, as the content of $NaNbO_3$ is increased from x=0.1 to x=0.7, the diffraction peaks corresponding to $NaNbO_3$ phase increases remarkably and the diffraction peaks corresponding to $BiFeO_3$ phase decreases gradually. The obvious peak splitting in the XRD spectrum shows the rhombohedral structure of nanoparticles, consistent with the structure of BFO ceramics.[23,27,28] The crystal structure changes from rhombohedral to orthorhombic by increasing the amount of $NaNbO_3$ phase in the composite.

The crystallite size was calculated from the full width at half maximum (FWHM) of the diffraction peaks using the Scherrer's equation. The calculated values of particle size are 6.2 nm, 10.9 nm , 41.7 nm and 79.2 nm for x=0, x=0.1, x=0.5 and x=0.7 respectively.

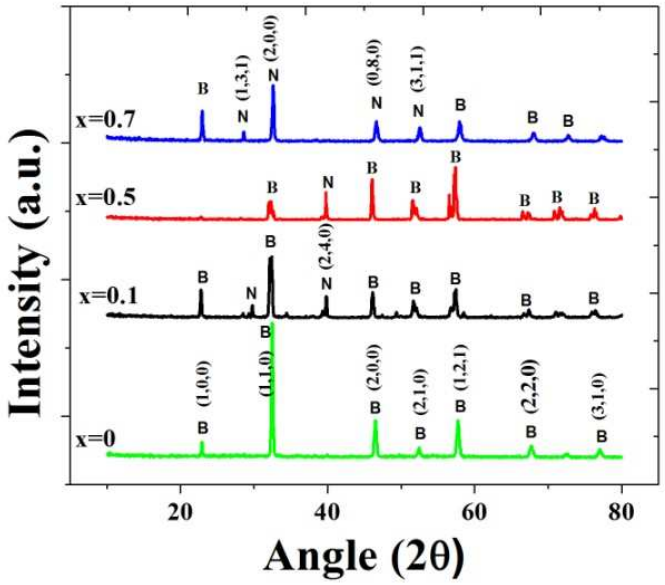

Fig. 1 XRD patterns of (1-x)$BiFeO_3$-x$NaNbO_3$ samples for x=0, 0.1, 0.5 and 0.7

A typical TEM image of the $BiFeO_3$-$NaNbO_3$ samples prepared by the present sol-gel method is shown in Fig. 2. HRTEM and SAED patterns of x=0.1, 0.5 and 0.7 are shown in Fig. 3. Both HRTEM and SAED pattern confirm the polycrystalline nature of the samples. The average particle size estimated from HRTEM images came out to be 6 nm, 10 nm, 43 nm and 80 nm for x=0, 0.1, 0.5 and 0.7 samples respectively and is consistent with the XRD analysis. The lattice spacing (d) calculated from the HRTEM image (fig. 3 (a)) matches with JCPDS values corresponding to $BiFeO_3$ and $NaNbO_3$. The d value 0.23 and 0.34 corresponds to (2,2,1) and (1,2,1) planes of orthorhombic $NaNbO_3$ (JCPDS 89-8957). Similarly d=0.39 corresponds to (1,0,0) plane of rhombohedral $BiFeO_3$ (JCPDS 74-2016). The SAED patterns show the presence of sharp diffraction spots, which is a clear indication of well developed, crystalline nanoparticles. The diffuse diffraction spots indicate the nanosize of the synthesized material.

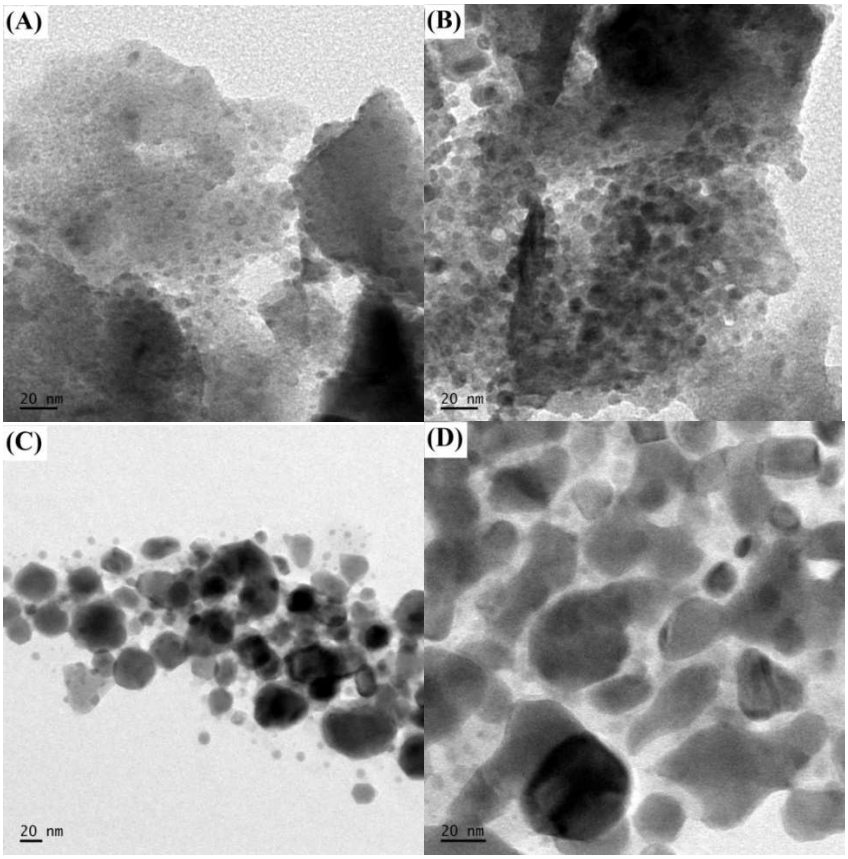

Fig. 2 TEM images of (1-x)$BiFeO_3$-x$NaNbO_3$ samples (a) for x=0, (b) for x=0.1, (c) for x=0.5, (d) for x=0.7 .

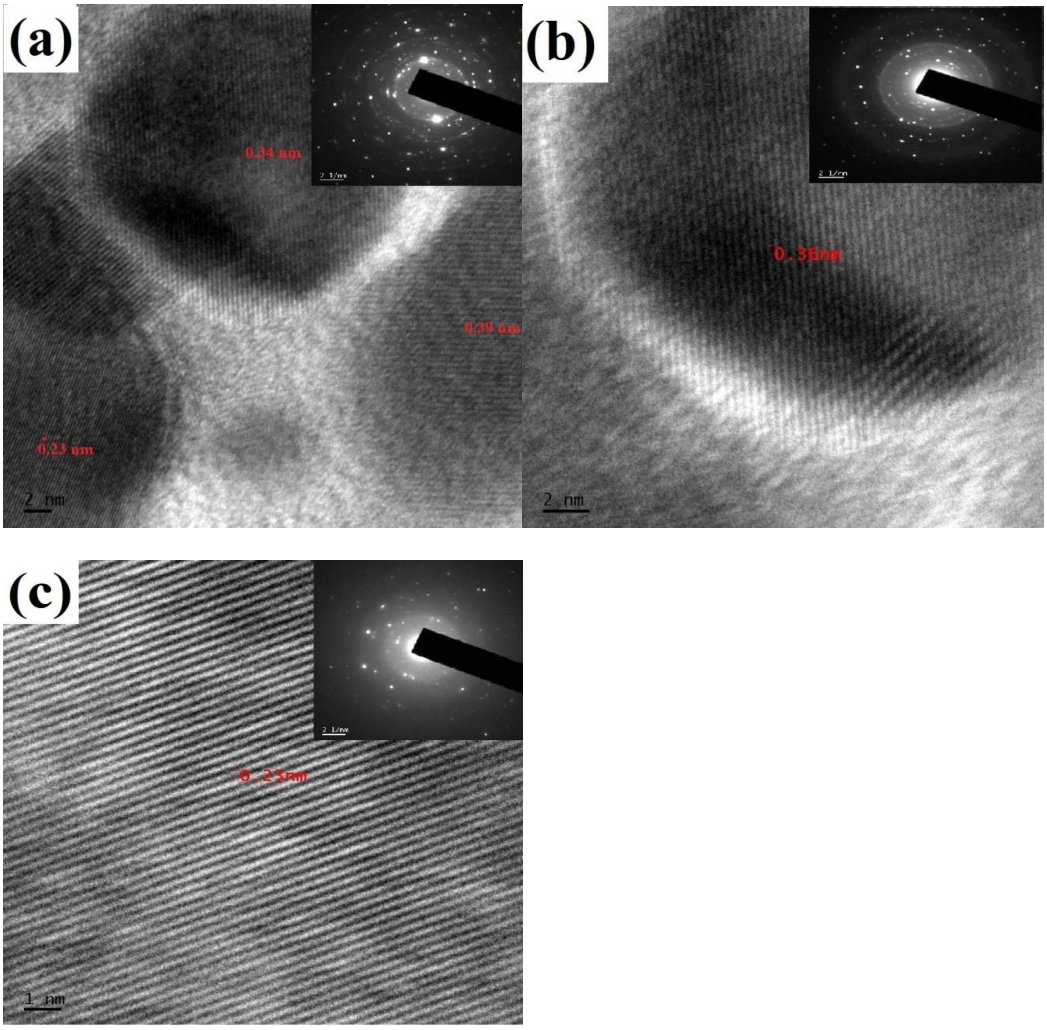

Fig. 3 HRTEM images of (1-x)$BiFeO_3$-x$NaNbO_3$ samples for (a) x=0.1, (b) x=0.5, (c) x=0. 7. Inset shows corresponding SAED patterns.

3.2 Electrical Studies

The frequency dependence of dielectric constant for (1-x)$BiFeO_3$ –x $NaNbO_3$ (x=0, 0.1, 0.5, 0.7) at room temperature in the frequency range 100 Hz to 2 MHz is shown in Fig. 4. The inset shows the dielectric loss (tan δ) with frequency. The variation of dielectric constant with frequency is very much consistent with that of other compounds/composites. It is evident that the dielectric constant and loss tangent decreases with increasing frequency. In the starting low frequency range both Ɛ and tan δ have higher values.

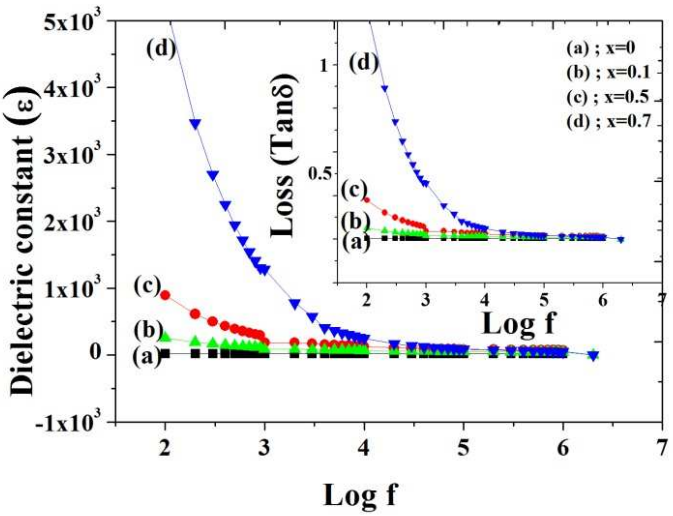

Fig. 4 The dielectric spectra of (1-x)$BiFeO_3$ –x $NaNbO_3$ samples (a) for x=0, (b) for x=0.1, (c) for x=0.5, (d) for x=0.7. (Inset shows the dielectric loss as a function of frequency).

The Ɛ and tan δ values decreases gradually as frequency increased from 100 Hz to 10 KHz and then decreases slowly and become almost constant up to 2 MHz for all compositions. The observations may be explained by the phenomenon of dipole relaxation.[29] The dielectric constant (Ɛ) of all the samples was found to decrease with increase of frequency in the low frequency region. This phenomenon can be attributed to the space charge relaxation effect. At low frequencies, the space charges are able to follow the frequency of the applied field, whereas these space charges do not find time to undergo relaxation at high frequency region.[28] At high frequency electric dipoles are unable to switch with frequency of the applied field. This is a general feature of dielectric materials.[22] It has been observed that at low frequency region, the dielectric constant is found to be dependent on different kinds of polarization (electronic, atomic, interfacial and ionic) whereas at high frequency region, only electronic polarization mainly contributes for the dielectric constant.[30] So there is a sharp decrease in dielectric constant at high frequency.[31] The values of the dielectric loss have been found to be very low at high frequencies and may find applications of these materials in high frequency microwave devices. The decrease of tan δ with increase in frequency can be explained on the basis of Koop's phenomenological theory.[32,33] The low losses may be attributed to the nanosized grains.[34,35] The low frequency dielectric dispersion increased with increase in $NaNbO_3$ concentration and it was maximum for

x=0.7. It should be noted that the dielectric constant is found to increase with increasing $NaNbO_3$ content. The dielectric constant is found to be increasing with decrease in particle size because of the presence of nanosized grains which act as a large insulating barrier for mobile charge carriers.[36] The dielectric constants of sol gel synthesized samples are very much higher as compared to solid state synthesized samples. It is clearly observed that sol-gel synthesized samples have very high value of dielectric constant in low frequency region in comparison with the previous reports on other rare earth doped $BiFeO_3$.[36-38]

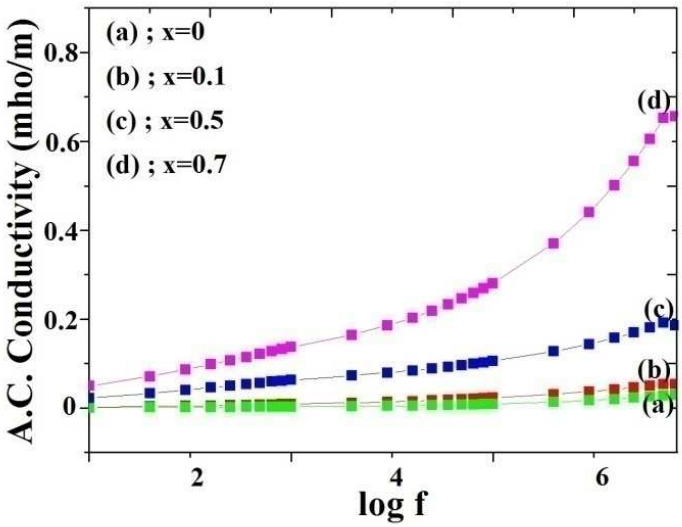

Fig. 5 A.C. conductivity of (1-x)$BiFeO_3$ –x $NaNbO_3$ samples (a) for x=0, (b) for x=0.1, (c) for x=0.5, (d) for x=0.7 .

AC conductivity studies were carried out for a better understanding of the frequency dependence of electrical property of the materials. Fig. 5 shows variation of AC conductivity as a function of frequency. The conductivity σ_{ac} was calculated using the dielectric data and empirical relation.

$$\sigma_{ac} = \omega\varepsilon_0\varepsilon_r \tan\delta. \qquad (1)$$

where ε_0 is the permittivity of free space and ω is the angular frequency. The conductivity curve shows that σ_{ac} increases with frequency which is a common feature of semiconductors.[36] The

increasing trend of σ_{ac} with frequency in the low frequency region might be attributed to the disordering of cations between neighboring sites and presence of space charges.[39]

3.3 Magnetic Studies

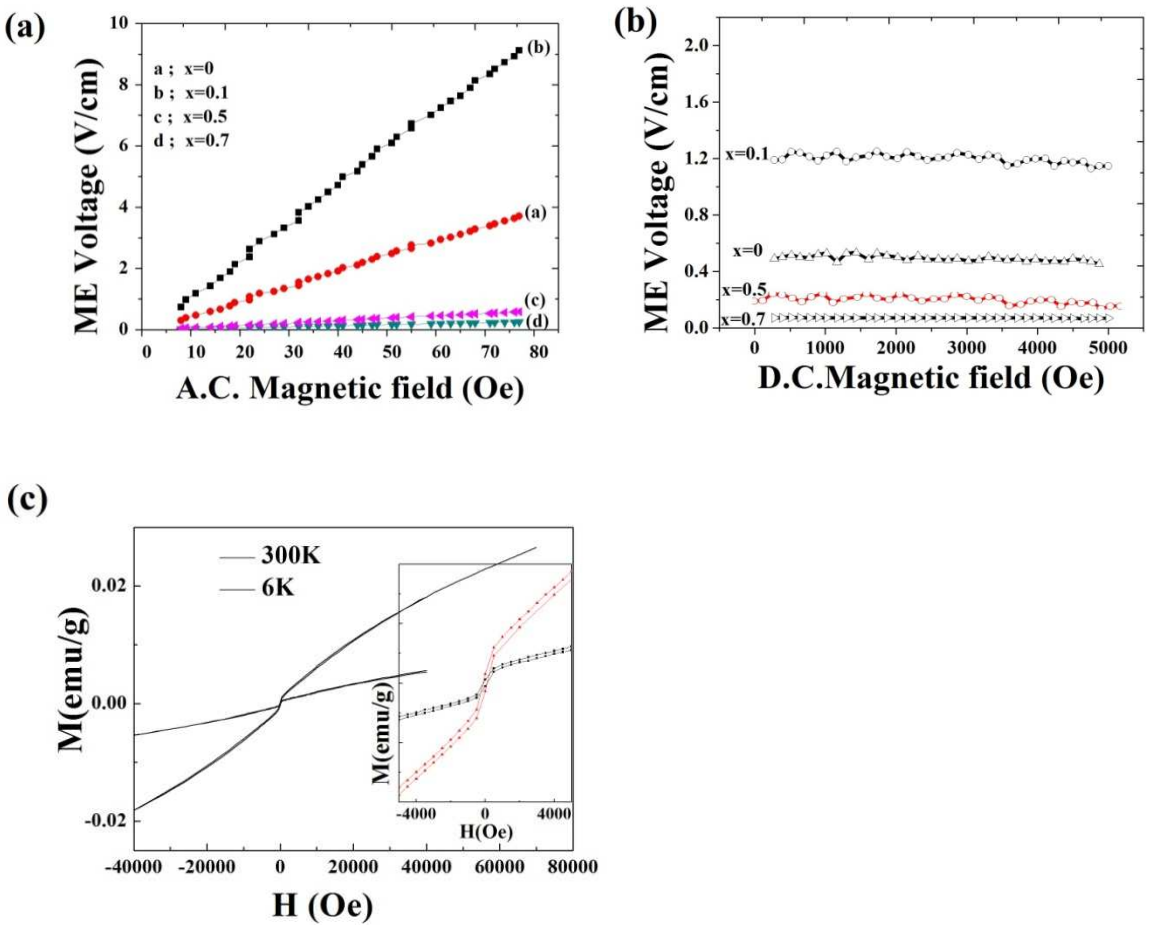

Fig. 6 (a) ME voltage as function of AC magnetic field, (b) ME voltage as a function of DC magnetic field, (c) Magnetization (M) versus magnetic field (H) plot of x=0.1 composition at 6K and 300 K (inset shows a zoomed view of the central portion).

The variations of ME voltage with AC and DC magnetic fields are plotted in Fig. 6 (a) and 6 (b) respectively. The ME output voltage measured up to 100 Oe (for Hac) shows linear increase with increasing magnetic field. When a magnetic field is applied to a magnetoelectric material, the material is strained. This strain induces a stress on the piezoelectric, which generates the electric field. This field could orient the ferroelectric domains, leading to an increase in polarization value. The magnetoelectric effect in multiferroics is fully described by the

magnetoelectric coupling coefficient. From the slope of the graph, coupling coefficient (α) is determined and it is found to be decreasing with increasing the $NaNbO_3$ content. The high value of ME coefficient, α =0.13 V/cmOe (for x=0.1) indicates the coexistence of electric and magnetic phases in this composition. To understand the magnetic behavior, the Magnetization (M) versus applied field (H) is measured for x=0.1 at two different temperatures (Fig. 6(c)). For bulk BFO the hysteresis loop is generally observed to be linear, indicating antiferromagnetic ordering of spins at the ground state. But here the hysteresis loop is similar to a typical weak ferromagnetic 'S' shaped curve. The small hysteresis loop observed at 6 K represents a soft magnetic phase with a low coercive field. It is found that the saturation is attained within the field of 40 kOe. The magnetic behavior at low temperature (6K) can be due to reduced particle size and absence of impurity. Also, numerous magnetization studies of antiferromagnetic nanoparticles have shown that the magnetization in large applied fields is considerably larger than that in the corresponding bulk materials. It was suggested by Neel that this might be due to the finite number of magnetic moments in nanoparticles, which may lead to a difference in the number of spin in the two sub lattices because of random occupancy of lattice sites. [40] This results in an uncompensated magnetic moment that leads to enhanced magnetic properties. At 300 K the hysteresis loop shows linear behavior which represents AFM ordering of spins characterestics of bulk BFO.[10,36]

3.4 Linear Optical studies

The UV-Visible absorption spectra of composites are shown in Fig. 7(a). The absorption cut-off wavelength of the as prepared composite samples lies between 500-600 nm which is close to the reported value for pure BFO (ie 560 nm),[23] suggesting that the present material can absorb visible light in the wavelength range of 400–565 nm. The UV-Visible absorption spectroscopy is frequently used to determine the energy bandgap of the powder samples from their absorption spectra. The optical band gap was determined from the Tauc plot (fig. 7.b)[42]. The tangent line, which is extrapolated to $(E\alpha)^2 = 0$, gives the bandgap (Eg).[42,43] The band gap values for each composite is shown in Table (1) which is in agreement with values from previous reports.[41] Pure $NaNbO_3$ have reported Eg value of 3.3-3.4 eV.[36] Incorporation of $NaNbO_3$ increases the band gap energy of the composite which is probably due to the interaction between $BiFeO_3$ and $NaNbO_3$.

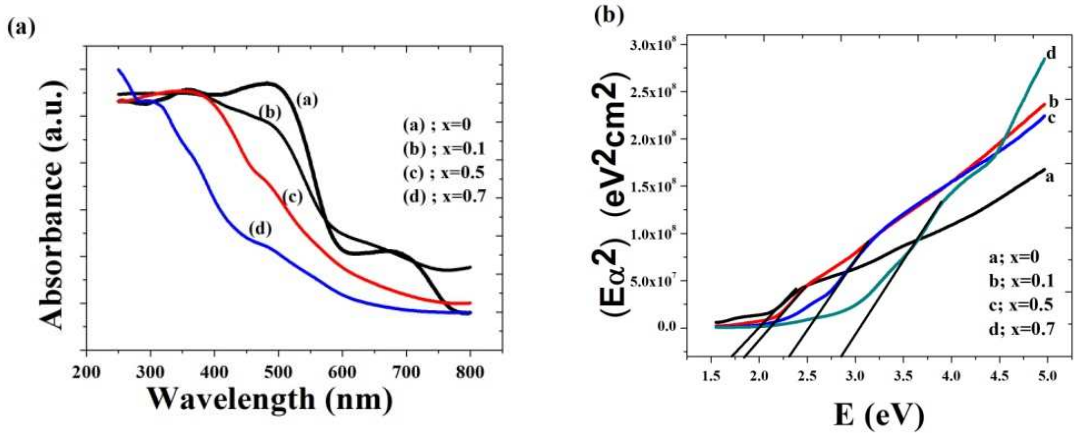

Fig. 7 (a) UV-VIS diffuse absorption spectra of the $BiFeO_3$-$NaNbO_3$ nanoparticles, where the dotted line is the division between UV and visible light. (b) Plot of $(E\alpha)^2$ versus photon energy (E).

Table 1: Bandgap energy of the samples

Sl. No	Sample name	Bandgap energy (eV)
1	X=0	1.7
2	X=0.1	1.9
3	X=0.5	2.3
4	X=0.7	2.8

3.5 Nonlinear Optical studies

The open aperture Z-scan curves (inset) and the corresponding intensity dependent transmissions calculated from the Z-scan curves, measured for ultrafast laser pulse excitation (800 nm, 100 fs) in the $BiFeO_3$-$NaNbO_3$ composites (for x=0, 0.1, 0.5, 0.7) are shown in Fig. 8, whereas those for short pulse excitation (532 nm, 5 ns) are shown in Fig. 9. The linear

transmission is adjusted to be about 65 % at both excitation wavelengths, and experiments were carried out at an average energy of 40 micro joules for nanosecond and 11 micro Joule for femtosecond excitations.

The open aperture Z-scan curves obtained in both cases exhibit a smooth valley indicating typical reverse saturable absorption behavior. In order to find the nature and strength of nonlinear absorption we numerically fitted the measured data to different nonlinear transmission equations. The best fit was obtained for a model in which 2PA (for fs excitation) or effective 2PA (for ns excitation) occurred along with SA.[44]

In such a case the nonlinear absorption coefficient can be written as

$$\alpha (I) = [\alpha_0/ (1+(I/I_s))]+ \beta I \qquad (2)$$

and the corresponding transmission equation is given by

$$dI/dz' = -[(\alpha_0/ 1+(I/I_s))+ \beta I]I \qquad (3)$$

This equation can be numerically solved to obtain the best fit values of saturation intensity (Is) and two photon absorption coefficient (β).

The calculated nonlinear parameters for short-pulse and ultrafast laser pulse excitations are presented in Table (2). The optical limiting performance is quantified using the optical limiting threshold value, which is defined as the input fluence at which the sample transmission drops to 50 % of its linear transmission.

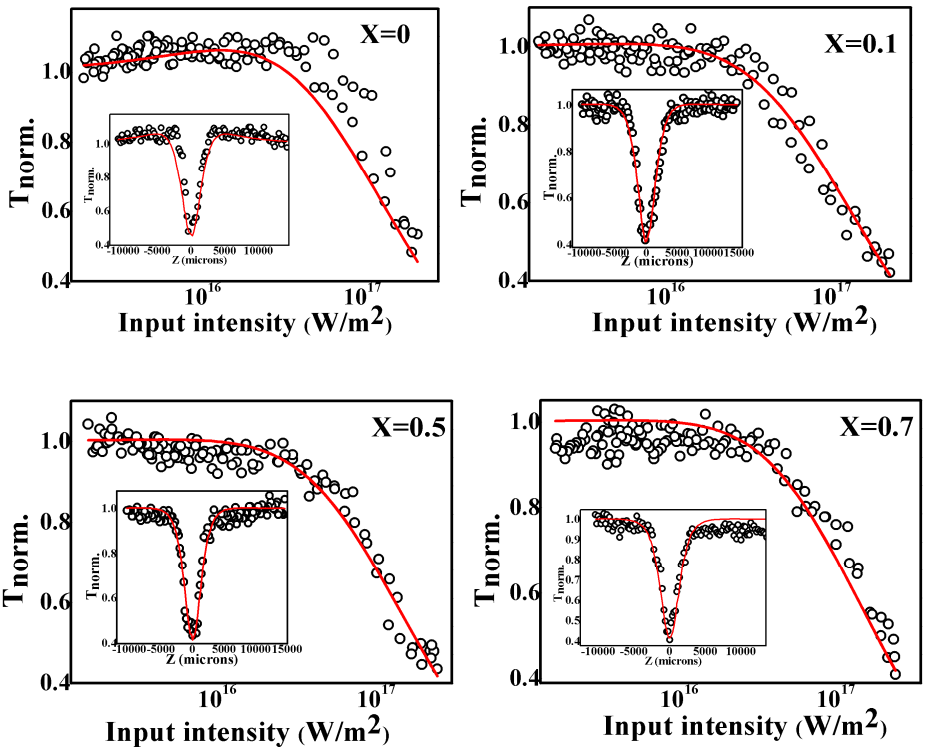

Fig. 8 Open aperture Z-scan curves (inset) and the corresponding intensity dependent normalized transmission obtained in $BiFeO_3$-$NaNbO_3$ (for x=0, 0.1, 0.5 and 0.7) for ultrafast (100 fs) pulse excitation. Open circles represents experimental data while the solid line represents numerical fit to Equation 3.

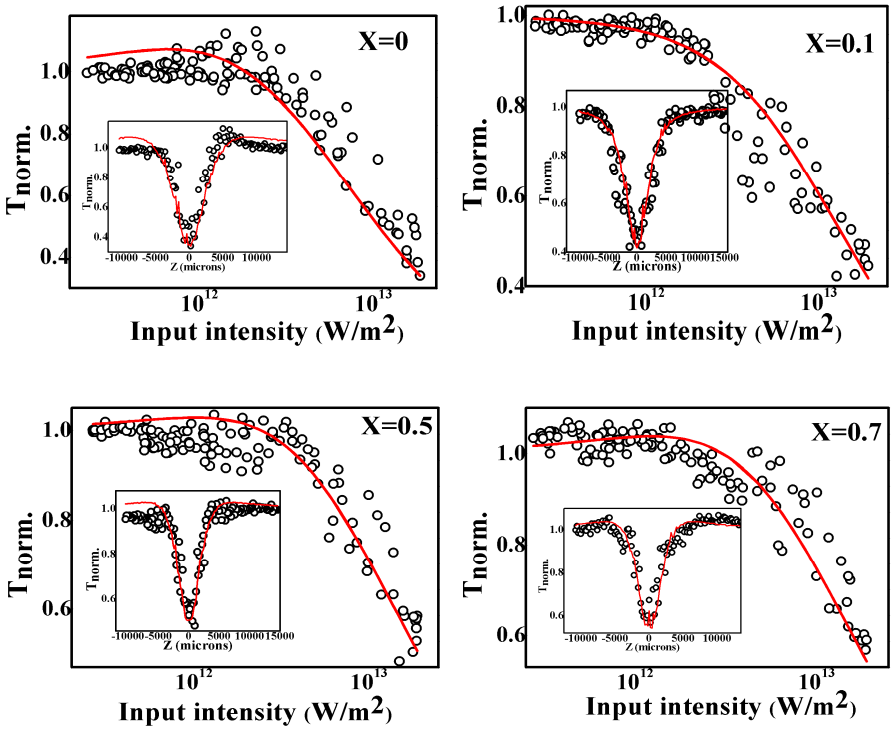

Fig. 9 Open aperture Z-scan curves (inset) and corresponding intensity dependent normalized transmission obtained in $BiFeO_3$-$NaNbO_3$ composites (for x=0, 0.1, 0.5 and 0.7) for 5 ns pulse excitation. Open circles represent experimental data while the solid line represents numerical fit to Equation 3.

Table 2: Calculated values of nonlinear optical parameters

Sl. No	Sample Name	5 ns excitation			100 fs excitation		
		B ($\times10^{-10}$m/w)	Is ($\times10^{11}$w/m^2)	Optical limiting threshold (J/Cm^2)	β ($\times10^{-14}$m/w)	Is ($\times10^{16}$w/m^2)	Optical limiting threshold (J/Cm^2)
1	X=0	1.8	7.99	1.1	1.1	2.0	1.7
2	X=0.1	1.2	5.499	1.4	1.1	3.0	1.7
3	X=0.5	1.0	2.499	1.9	1.0	3.4	1.8
4	X=0.7	0.9	2.499	2.2	1.0	3.6	1.9

Z-scan experiments with relatively long (5 ns) laser pulses allow for multiple absorption from the same laser pulse, which greatly enhances excited state absorption (ESA). While the incorporation of $NaNbO_3$ into $BiFeO_3$ provides no significant modification to the ultrafast optical nonlinearity of $BiFeO_3$, it obviously affects the nanosecond optical nonlinearity (Fig. 9). In this case nonlinear absorption is found to decrease with increase in the $NaNbO_3$ concentration. This quenching of nonlinear optical absorption in the composite originates from factors associated with size reduction such as increase in grain boundaries and increase in the energy gap by increasing the $NaNbO_3$ content. Pure $BiFeO_3$ has an Eg of 1.72 eV, but the incorporation of $NaNbO_3$ into $BiFeO_3$ results in an increase in band gap energy to 2.53 eV when x=0.7.

4. Conclusion

Phase pure $BiFeO_3$-$NaNbO_3$ nanocomposite samples were successfully synthesized using Pechini method. XRD and TEM analysis show that all the particles are in the nanometer size and no secondary phases were formed during the synthesis. The reduced size and absence of impurity could be the reason for high dielectric constant and good ME coupling. For the selected composition (x=0.1) improved magnetization is found in the hysteresis loop and we obtained reduced Eg values for the samples. The reduced band gap and reduction in particle size is found as the reason for enhanced nonlinear optical properties of the present set of samples compared to their bulk form. From exciting the samples using nanosecond and femtosecond laser pulses we conclude that 2PA and effective 2PA are the dominant absorptive nonlinearities in the present set of samples. These samples exhibit efficient optical limiting and can have potential applications in photonic devices.

Acknowledgement

The authors would like to acknowledge the financial support from DST – Govt. of India through the Nano Mission, PURSE, FIST Programs, and UGC – Govt. of India for the SAP program.

References

1. Ruimin Yao, Chuan Bao Cao, Chunrui Zheng Qiang Lei, RSC Adv, 2013, 3, 24231-24236.
2. B. Raneesh, A. Saha, D. Das, R. Sreekanth, R. Philip, Nandakumar Kalarikkal, RSC Adv, 2015, 5, 12480.
3. J. Hemberger, P. Lunkenheimer, R. Fichtl, H.A. Nidda, V. Tsurkan and A. Loidl, Nature, 2005 434, 364.
4. Jeevan Job Thomas, Shiji Krishnan, K. Sridharan, Reji Philip, Nandakumar Kalarikkal, Materials Research Bulletin, 2012, 47, 1855–1860.
5. Jeevan Job Thomas, A. B. Shinde, P. S. R. Krishna, Nandakumar Kalarikkal, Journal of Alloys and Compounds, 2013, 546, 77–83.
6. J. Hemberger, P. Lunkenheimer, R. Fichtl, H. A. Nidda, V. Tsurkan and A. Loidl, Nature, 2005 434, 364.
7. N. A. Hill, J. Phys. Chem. B, 2000, 104, 6694.
8. W. Eerenstein, N. D. Mathur and J. F. Scott, Nature, 2006, 442, 759.
9. J. H. Xu, H. Ke, D. C. Jia, W. Wang and Y. Zhou, J. Alloys Compd, 2009, 472.
10. Valdirlei F. Freitas, Ot´avio A. Protzek, Luciano A. Montoro, Andre M. Gonçalves, Ducinei Garcia, Jose A. Eiras, Ruyan Guo, Amar S. Bhalla, Luiz F. Coticaad and Ivair A. Santos, J. Mater. Chem. C, 2014, 2, 364.
11. S. R. Basu, L. W. Martin, Y. H. Chu, M. Gajek, R. Ramesh, R. C. Rai, X. Xu and J. L. Musfeld, Appl. Phys. Lett, 2008, 92, 091905.
12. A. J. Hauser, J. Zhang, L. Mier, R. A. Ricciardo, P. M. Woodward, T. L. Gustafson, L. J. Brillson and F. Y. Yang, Appl. Phys. Lett, 2008, 92, 222901.
13. Guoqiang Li, Zhiguo Yi, Ying Bai, Weifeng Zhang and Haitao Zhang, Dalton Trans, 2012, 41, 10194–10198.
14. Antonio Perejon, Pedro E. Sanchez-Jimenez, Luis A. Perez-Maqueda, J. Mater. Chem. C, 2014, 2, 8398.
15. B. Raneesh, H. Soumya, J. Philip, S. Thomas, K. Nandakumar, Journal of Alloys and Compounds, 2014, 611, 381–385.
16. B. Y. Wang, H. T. Wang, Shashi B. Singh, Y. C. Shao, **RSC Adv**, 2013, **3**, 7884-7893.
17. C. A. F. Vaz, J. Hoffman, C. H. Ahn, and R. Ramesh, Adv. Mater, 2010, 22, 2900–2918.

18. Y. Ma and X. M. Chen. J. Appl. Phys, 2009, 105, 054107.
19. E. Hollenstein, M. Davis, D. Damjanovic, N. Setter, Appl. Phys. Lett, 2005, 87.
20. G. A. Smolenski, V. A. Bokov, V. A. Isupov, N. N. Krainink, R. E. Pasynkov and A. I. Sokolov, Ferroelectric and related materials, Gordon and Breach Sci. Publishers, New York, (1984).
21. Chia Ching Wua and Cheng Fu Yang, Cryst. Eng. Comm, 2013, 15, 9097–9103.
22. H. O. Rodrigues, G. F. M. Pires, Jr., J. S. Almeida, E. O. Sancho, A. C. Ferreira, M. A. S. Silva, and A. S. B. Sombra, J. Phys. Chem. Solids, 2010, 71, 1329.
23. S. T. Zhang, M. H. Lu, D. Wu, Y. F. Chen and N. B. Ming, Appl. Phys. Lett, 2005, 87, 262 907.
24. Shiji Krishnan, Nandakumar Kalarikkal, J Sol-Gel Sci.Technol, 2013, 66, 6–14.
25. I. P. Raevski, S. P. Kubrin, J. L. Dellis, S. I. Raevskaya, D. A. Sarychev, V. G. Smotrakov, Ferroelectrics, 2008, 371, 113-118.
26. S. X. Huo, S. L. Yuan, Y. Qiu, Z. Z. Ma, C. H. Wang, J. Material letters, 2012, 68, 8-10.
27. Sheng Ju, Tian Yi Cai, Guang Yu Guo, The journal of chemical physics, 2009, 130, 214708.
28. M. Kumar, K. L. Yadav, J. Phys. Condense. Matter, 2007, 19, 242202.
29. Guoqiang Li, T. Kako, D. Wang, Z. Zou, J. Ye, J. Phys. Chem. Solids, 2008, 69, 2487.
30. J. C. Anderson, Dielectrics, Chapman & Hall, 1964, London, Vol 1.
31. D. R. Patil, S. A. Lokare, R. S. Devan, S. S. Chougule, C. M. Kanamadi, Y. D. Kokekar, and B. K. Chougule, Mater. Chem. Phys., 2007, 104, 254.
32. B. Kumari, P. R. Mandal, T. K. Nath, Adv. Mat. Lett, 2014, 5, 2.
33. S. R. Kulkarni, J. Phys. Chem. Sol, 2006, 67, 1607.
34. C. G. Koops, Phys. Rev, 1951, 83, 121.
35. Qian, F. Z. Jiang, J. S. Guo, S. Z. Jiang, D. M. Zhang, J. Appl. Phys., 2009, 106, 084312.
36. Yi Du, Cheng Z. X, Shahbazi M, Collings E W, Dou S X, Wang X L, J. Alloy. Compd.2010, 490, 637.
37. Gitanjali Dhir, Poonam Uniyal, N. K. Verma, J. Supercond, 2014, 27.
38. Sen K, Singh K, Gautam A, Singh M, Cera inter, 2012, 38, 243.

39. A. K. Jonscher, Dielectric Relaxation in Solids, Chelsca Dielectric Press Limited, London, 1986.
40. Neel L, Magnetic nanoparticle Assemblies, CBC press, Taylor and Francis group, 1961, Vol 1, Ch 2, pp 253
41. B. Bhushan, A. Basumallick, S. K. Bandopadhyay, N. Y. Vasanthacharya and D. Das, J. Phys. D Appl. Phys, 2009, 42, 065004.
42. J. Tauc, Amorphous And Liquid Semiconductors, Plenum Press, New York, 1974,Vol 1, Ch 4, pp239.
43. Y. Kim, S. J. Atherton, E. S. Brigham and T. E. Mallouk, J. Phys. Chem., 1993,97, 11802.
44. B. Karthikeyan, M. Anija, P. Venkatesan, C. S. Suchand Sandeep, R. Philip, Opt.Commun. 2007, 280, 482.

Figure captions

Fig. 1: XRD patterns of (1-x)$BiFeO_3$-x$NaNbO_3$ samples for x=0, 0.1, 0.5 and 0.7

Fig. 2: TEM images of (1-x)$BiFeO_3$-x$NaNbO_3$ samples (a) for x=0, (b) for x=0.1, (c) for x=0.5, (d) for x=0.7 .

Fig. 3: Fig. 3 HRTEM images of (1-x)$BiFeO_3$-x$NaNbO_3$ samples for (a) x=0.1, (b) x=0.5, (c) x=0. 7. Inset shows corresponding SAED patterns.

Fig. 4: The dielectric spectra of (1-x)$BiFeO_3$ –x $NaNbO_3$ samples (a) for x=0, (b) for x=0.1, (c) for x=0.5, (d) for x=0.7 . (inset shows loss).

Fig. 5: A.C. conductivity of (1-x)$BiFeO_3$ –x $NaNbO_3$ samples (a) for x=0, (b) for x=0.1, (c) for x=0.5, (d) for x=0.7 .

Fig. 6: (a) ME voltage as function of AC magnetic field, (b) ME voltage as a function of DC magnetic field, (c) Magnetization (M) versus magnetic field (H) plot of x=0.1 composition at 6K and 300 K (inset shows a zoomed view of the central portion).

Fig. 7: (a) UV-VIS absorption spectra of the $BiFeO_3$-$NaNbO_3$ nanoparticles, where the dotted line is the division between UV and visible light. (b) Plot of $(E\alpha)^2$ versus photon energy (E).

Fig. 8: Open aperture Z-scan curves (inset) and the corresponding intensity dependent normalized transmission obtained in $BiFeO_3$-$NaNbO_3$ (for x=0, 0.1, 0.5 and 0.7) for ultrafast (100 fs) pulse excitation. Open circles represents experimental data while the solid line represents numerical fit to equation 3.

Fig. 9: Open aperture Z-scan curves (inset) and corresponding intensity dependent normalized transmission obtained in $BiFeO_3$-$NaNbO_3$ composites (for x=0, 0.1, 0.5 and 0.7) for 5 ns pulse excitation. Open circles represent experimental data while the solid line represents numerical fit to equation 3.

Table captions

Table 1 Bandgap energy of the samples

Table 2 Calculated values of nonlinear optical parameters